Vortex breakdown control by adding near-axis swirl and temperature gradients

Miguel Angel Herrada*
Escuela Superior de Ingenieros, Universidad de Sevilla, 41092 Sevilla, Spain

Vladimir Shtern
Department of Mechanical Engineering, University of Houston, Houston, Texas 77204-4006, USA
(Received 2 June 2003; published 14 October 2003)

Vortex breakdown (VB) is an intriguing effect of practical and fundamental interest, occurring, e.g., in tornadoes, above delta-wing aircraft, and in vortex devices. Depending on application, VB is either beneficiary or harmful and therefore requires a proper control. This study shows that VB can be efficiently controlled by a combination of additional near-axis swirl and heat. To explore the underlying mechanism, we address a flow in a cylindrical container driven by a rotating bottom disk. This model flow has been extensively studied being well suited for understanding both the VB mechanism and its control. Our numerical analysis explains experimentally observed effects of control corotation and counter-rotation (with no temperature gradient) and reveals some flaws of dye visualization. An important feature found is that a moderate negative (positive) axial gradient of temperature can significantly enforce (diminish) the VB enhancement by the counter-rotation. A strong positive temperature gradient stimulates the centrifugal instability and time oscillations in the flow with counter-rotation. An efficient time-evolution code for axisymmetric compressible flows has facilitated the numerical study.

DOI: 10.1103/PhysRevE.68.041202 PACS number(s): 47.10.+g, 47.32.−y, 83.85.Pt

I. INTRODUCTION

Vortex breakdown is an intriguing and practically important phenomenon occurring in many natural and technological swirling flows. These flows have a vortex core—a thin (compared with the flow scale) and axially elongated region where swirl is of the solid-body type and vorticity has a sharp peak. Under some circumstances, the core abruptly expands into a bubblelike circulatory zone or into a helical or multihelical pattern. This transformation is a *vortex breakdown* (VB).

VB has been observed over delta wings of aircraft [1], in tornadoes [2], in vortex burners and other technological devices [3]. VB on a delta wing causes an abrupt drop in lift, an increase in drag, and the development of a rolling moment; these effects can lead to the loss of aircraft control [4]. In contrast, VB is desirable in vortex burners, providing stable combustion with VB bubbles acting as flame holders [3]. VB in a tornado decreases its swirl velocity and thus makes the tornado less destructive [5]. Thus, the VB control—either suppression or enhancement—is of practical importance.

VB is also of theoretical interest: despite more than four decades of extensive studies, there is no consensus on what constitutes VB, let alone on its mechanism. A few competing theories attempt to explain VB [6], and much experimental and numerical work has been done to clarify its nature. Fundamental studies of VB often employ a flow in a cylindrical container. This confined flow has the following important advantages: (i) absence of unpredictable ambient disturbances, (ii) well-defined boundary conditions, and (iii) precise variation of control parameters. These features facilitate both well-organized experiments and well-posed problems for numerical simulations, as well as a detailed comparison of experimental and numerical results. In particular, the container flow driven by a rotating disk is the subject of a number of experimental [7–9] and numerical [10–12] works. An understanding of the physics and the VB control can then be extended to practical flows, confined or open.

In recent studies, two means of VB control have been proposed: a rotation of a near-axis rod [13] and an axial temperature gradient [14]. The numerical simulations made here clarify the mechanism of VB control experimentally investigated in Ref. [13] and show that a combination of rotational and thermal means can provide even more efficient VB control. To this end, a new powerful time-evolution code for compressible flows has been developed.

Compressibility effects are twofold: kinematic (characterized by the Mach number Ma) and buoyant (due to temperature-induced density variations). The Ma-related effect being important for the VB development in pipe flows [15,16] is negligible for the VB flow in a closed container when $\mathrm{Ma}<0.5$ [14]. In contrast, the effect of buoyancy is so strong here that it does not permit use of the Boussinesq approximation.

In the remainder of the paper we formulate the problem (Sec. II), describe a new numerical code (Sec. III), study the VB control by near-axis swirl and thermal convection in a container flow driven by rotation of the bottom disk (Sec. IV), and summarize the results (Sec. V).

II. PROBLEM FORMULATION

A. Governing equations

We use the Navier-Stokes equations for a compressible axisymmetric flow in the form

*Email address: herrada@eurus2.us.es

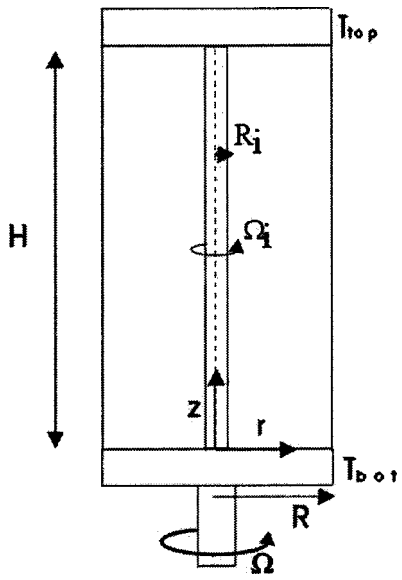

FIG. 1. Schematic of the problem.

$$\frac{D\rho}{Dt} = -\rho\Delta, \tag{1}$$

$$\rho\frac{Du}{Dt} = \rho\frac{v^2}{r} - \frac{1}{M^2}\frac{\partial p}{\partial r} + \frac{1}{\mathrm{Re}}\left(\nabla^2 u - \frac{u}{r^2} + \frac{\partial\Delta}{\partial r}\right), \tag{2}$$

$$\rho\frac{Dv}{Dt} = \rho\frac{vu}{r} + \frac{1}{\mathrm{Re}}\left(\nabla^2 v - \frac{v}{r^2}\right), \tag{3}$$

$$\rho\frac{Dw}{Dt} = -\frac{1}{M^2}\frac{\partial p}{\partial z} + \frac{1}{\mathrm{Re}}\left(\nabla^2 w + \frac{\partial\Delta}{\partial z}\right), \tag{4}$$

$$\frac{Dp}{Dt} = -3\gamma p\Delta + \frac{\gamma-1}{\gamma\mathrm{Pr}\,\mathrm{Re}}(\nabla^2 T) + \frac{\gamma-1}{\gamma\,\mathrm{Re}}\mathrm{Ma}^2\Phi, \tag{5}$$

$$p = \rho T, \tag{6}$$

where $D/Dt \equiv \partial/\partial t + u\partial/\partial r + w\partial/\partial r$, $\nabla^2 \equiv r^{-1}\partial(r\partial/\partial r)/\partial r + \partial^2/\partial^2 z$, $\Delta \equiv [r^{-1}\partial(ru)/\partial r + \partial w/\partial z]/3$, and $\Phi = 2[(\partial u/\partial r)^2 + (u/r)^2 + (\partial w/\partial z)^2] + (\partial u/\partial z + \partial u/\partial r)^2 + (\partial v/\partial r - v/r)^2 + (\partial v/\partial z)^2 - 6\Delta^2$.

Here $\{u,v,w\}$ are the velocity components in cylindrical coordinates $\{r,\theta,z\}$ (Fig. 1), p is the pressure, ρ is the fluid density, and T is the temperature. We have made all variables dimensionless by using the following scales: R for length, $1/\Omega$ for time, ΩR for velocity, T_0 for temperature, ρ_0 for density, and $R_g\rho_0 T_0$ for pressure; R is the radius of the cylindrical container, Ω is the angular velocity of the rotating bottom disk (Fig. 1), T_0 and ρ_0 are initial values of temperature and density when the fluid is at rest, and $R_g = (c_p - c_v)$ is the gas constant.

Dimensionless parameters in Eqs. (1)–(6)—$h = H/R$, $\mathrm{Re} = \rho_0\Omega R^2/\mu$, $\mathrm{Ma} = \Omega R(\rho_0 R_g T_0)^{-1/2}$, $\mathrm{Pr} = \rho_0 c_p/\lambda$, and $\gamma = c_p/c_v$—are the aspect ratio (H is the cylinder height), the Reynolds, Mach, and Prandtl numbers, and specific heat ratio, respectively. Viscosity μ, thermal conductivity λ, and the specific heats c_p and c_v are kept constant in our analysis. We take $\mathrm{Pr} = 0.72$ and $\gamma = 1.4$ as values typical of gases.

The base flow is controlled by a rotation of the central rod and the axial gradient of temperature. The control rotation is characterized by the Reynolds number $\mathrm{Re}_i = \rho_0\Omega_i R_i^2/\mu$ based on the radius R_i and on the angular velocity Ω_i of the rotating rod. The thermal control is characterized by the dimensionless temperature difference, $\varepsilon = (T_{\mathrm{bot}} - T_{\mathrm{top}})/(T_{\mathrm{bot}} + T_{\mathrm{top}})$, where T_{bot} and T_{top} are the temperatures of the bottom and top disks; $T_0 = (T_{\mathrm{bot}} + T_{\mathrm{top}})/2$.

B. Initial and boundary conditions

Integration of Eqs. (1)–(6) runs from $t = 0$ when the fluid is at rest and has a uniform temperature and density, with

$$u(r,z,0) = v(r,z,0) = w(r,z,0) = 0,$$

$$T(r,z,0) = \rho(r,z,0) = 1. \tag{7}$$

Then we set the bottom disk and the rod to rotate and impose an axial gradient of temperature at the container wall. Therefore, the boundary conditions are

$$u(r,0,t) = w(r,0,t) = 0, \quad v(r,0,t) = r, \quad T(r,0,t) = 1+\varepsilon \tag{8}$$

at the bottom disk ($z = 0$),

$$u(r,h,t) = w(r,h,t) = 0, \quad v(r,h,t) = 0, \quad T(r,h,t) = 1-\varepsilon \tag{9}$$

at the top disk ($z = h$), and

$$u(1,z,t) = w(1,z,t) = 0, \quad v(1,z,t) = 0, \quad T(1,z,t) = 1+\varepsilon - 2\varepsilon z/h \tag{10}$$

at the sidewall ($r = 1$).

Finally, at the rotating rod ($r = r_i = R_i/R$)

$$u(r_i,z,t) = w(r_i,z,t) = \partial T/\partial r(r_i,z,t) = 0,$$

$$v(r_i,z,t) = \mathrm{Re}_i/(r_i\,\mathrm{Re}). \tag{11}$$

Equations (1)–(6) together with conditions (7)–(11) formulate a closed mathematical problem.

III. NUMERICAL PROCEDURE

The spectral method [17] appears to be more efficient than a finite difference or finite element approximation for spatial variables, because it resolves thin boundary layers typical of the flow addressed with relatively few collocation points. In addition, spectral methods can be easily applied here due to the simplicity of the computational domain. We integrate Eqs. (1)–(6) under conditions (7)–(11) using 61×61 spectral Chevychev collocation points [17] in the physical space. With this resolution, our results (at $\mathrm{Re} = 2700$, $\mathrm{Re}_i = 0$, $\varepsilon = 0$, $r_{\mathrm{in}} = 0$, $h = 2.5$) are very close to those obtained in Ref. [14] by using a compact Padé scheme in space [18] with a mesh with 121×301 points.

The explicit time advancement is performed by using a fourth-order low-storage Runge-Kutta method [19]. In all the cases considered, a characteristic time of a remarkable variation of any physical quantity involved is much larger than a time step. We use a small time step (specified below) to guarantee the numerical stability of the explicit time procedure used. Since the required time step drastically decreases with the Mach number, we use a moderate value of Ma $(=0.3)$ to save the calculation time. Here we exploit the fact that the effect of the Mach number for this kind of flow is negligibly small in the range $0 \leqslant \mathrm{Ma} \leqslant 0.5$. This allowed us to use time step Δt from the interval (0.005, 0.007).

We would like to emphasize that our code for a compressible fluid does not involve the Boussinesq approximation. A reason is that variations of temperature and density are not small here. The numerical scheme, although being nonconservative (and therefore not applicable for supersonic flows), works quite satisfactorily for the well subsonic flow considered.

IV. RESULTS

A. Vortex breakdown control by adding near-axis rotation

Using the code described above, we first compare our numerical results with experimental observations [13] of the flow controlled by the corotating or counter-rotating rod with no thermal control. Also we investigate speculations made in Ref. [13] by calculating relevant flow characteristics. To this end, we take the same parameters as those in Ref. [13]: $h=3.25$, $\mathrm{Re}=2720$, $r_i=0.04$ and first apply no temperature gradient $(\varepsilon=0)$.

Figure 2 shows streamline patterns by (a) flow visualization [13] and (b) our calculation of the flow where the rod is at rest $(\mathrm{Re}_i=0)$. Although the Mach number used in the numerical simulation $(\mathrm{Ma}=0.3)$ is a few orders of magnitude larger than that in the experiment $(\mathrm{Ma}\sim 10^{-3})$, the results are close. A minor difference is that the visualization seems to show three vortex rings [Fig. 2(a)] while the numerical results reveal only two vortex rings [Fig. 2(b)]. In numerical simulations, the stream function is zero at walls and vortex-ring boundaries (being negative inside vortex rings and positive outside). This feature helps us to unambiguously determine whether a vortex ring occurs in the flow. To visualize vortex rings, we plot at least one streamline inside each ring.

To check whether this disagreement is due to the different Ma values, we have performed calculations at $\mathrm{Ma}=0.1$ and, in addition, by using a different code for an incompressible fluid, at $\mathrm{Ma}=0$. These three runs—for $\mathrm{Ma}=0$, 0.1, and 0.3—yielded very close streamline patterns all with two vortex rings only. We conclude that there is another reason for the disagreement and explore one conjecture below.

Figure 2(b) shows that streamlines are wavy in the region where the bubble (ii) is visualized in Fig. 2(a). Our calculations yield that the flow is nearly stagnant in the near-axis core of the wavy region. Therefore, the Fluorecein dye can fill this nearly stagnant region and thus mimic a vortex-breakdown ''bubble'' in the experiment.

This conjecture is consistent with the results presented in Fig. 3 for the flow at $\mathrm{Re}_i=21$ (corotating rod). According to

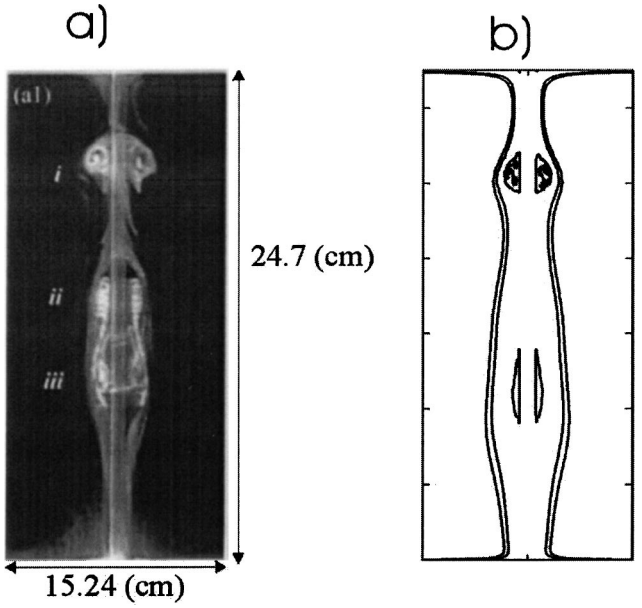

FIG. 2. Comparison of (a) experimental [13] and (b) numerical results at $\mathrm{Re}=2720$, $\mathrm{Re}_i=0$, and $ri=0.04$. $R=7.62$ cm, $H=24.7$ cm. Contours in (b) are solid (broken) for positive (negative) stream function and show ten stream function (ψ) values: contours $+$, $\psi=0.01\times\psi_{\max}\times(i-1)/2$, $i=1$, 3; contours $-$, $\psi=i\times\psi_{\min}/5$, $i=1$, 8, $\psi_{\max}=0.0069$, and $\psi_{\min}=-5\times10^{-6}$.

the numerical results, two vortex rings shown in Fig. 2(b) are completely suppressed in Fig. 3(b), but streamlines remain wavy in the former-vortex-ring regions with nearly stagnant zones near the axis. These zones also can accumulate the dye resulting, e.g., in bubble (i) in Fig. 3(a) [13]. Therefore, a flow pattern interpreted as a bubble from the dye visualization might be not a bubble at all, except those identified in both the experiment [13] and our calculation.

Despite these minor differences, the numerical and experimental results well agree concerning the main effect—

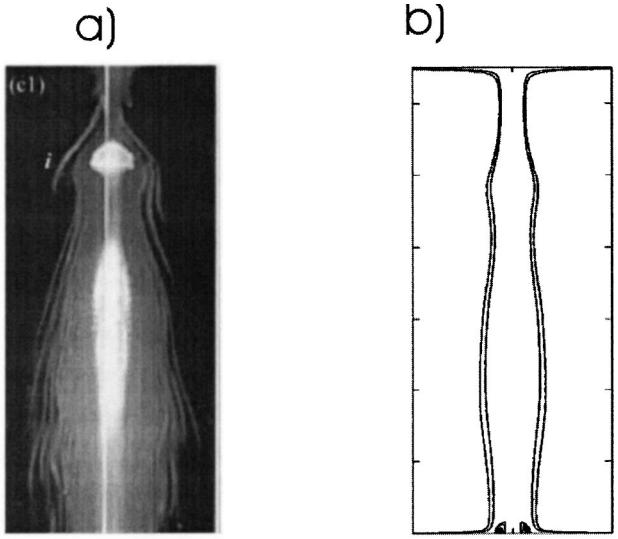

FIG. 3. As in Fig. 2, but at $\mathrm{Re}_i=21$. Contours $+$: $\psi=0.01\times\psi_{\max}\times(i-1)/2$, $i=1$, 3; contours $-$: $\psi=i\times\psi_{\min}/5$, $i=1$, 8, $\psi_{\max}=0.0069$, and $\psi_{\min}=-6.2\times10^{-6}$.

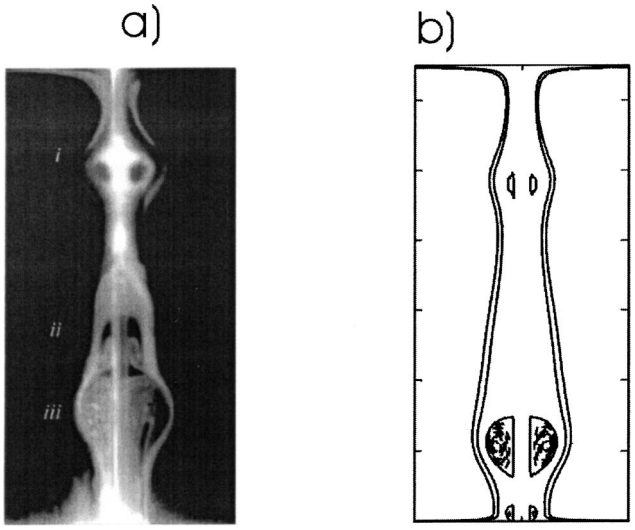

FIG. 4. As in Fig. 2, but at $\mathrm{Re}_i=-12$. Contours +: $\psi=0.01\times\psi_{\max}\times(i-1)/2$, $i=1$, 3; contours −: $\psi=i\times\psi_{\min}/5$, $i=1$, 8, $\psi_{\max}=0.0068$, and $\psi_{\min}=-1.04\times10^{-5}$.

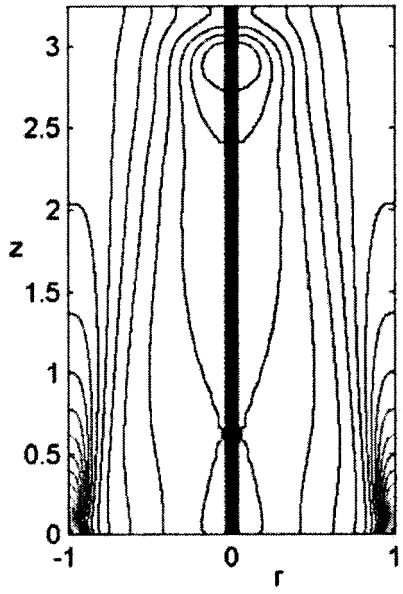

FIG. 5. Pressure contours at $\mathrm{Re}=2720$, $\mathrm{Re}_i=0$, $h=3.24$, and $r_i=0.04$. Contours are for 41 pressure values: $p=p_{\min}+(p_{\max}-p_{\min})(i-1)/40$; $i=1,41$, $p_{\min}=1.0002$, and $p_{\max}=1.0062$.

suppression of vortex breakdown even by a weak co-rotation of the rod. Now we address the flow with the rod counter-rotation.

Figure 4 compares the experimental and numerical results at $\mathrm{Re}_i=-12$ (negative Re_i correspond to the counter-rotating rod). These results are in excellent agreement both showing that the counter-rotation (a) significantly enlarges the vortex ring (iii), (b) shifts the vortex ring (iii) downstream, and (c) the flow is still steady at this Re_i.

An advantage of a simulation is that it is capable of providing numerical values of any quantity of physical interest. In particular, we can check the speculation made in Ref. [13] concerning the role of pressure in the vortex-breakdown occurrence. To this end, Fig. 5 depicts pressure contours for the flow shown in Fig. 2 ($\mathrm{Re}_i=0$). Husain *et al.* [13] supposed that pressure is nearly constant along the sidewall. In contrast, our calculations reveal that pressure significantly varies along the sidewall. Fortunately, Fig. 5 also shows a region in between the sidewall and the rod where pressure contours are nearly parallel to the sidewall, i.e., pressure is nearly z independent in this region. Therefore, the speculation made in Ref. [13] is valid if this in-between region can serve as the periphery (where $p\approx p_\infty$) of the near-axis vortex core.

Figure 6 depicts the pressure distribution along the rod surface as a function of z for the Re_i values shown near the curves. The large positive gradient of pressure observed near the top accelerates the near-axis flow. As z decreases, the pressure reaches its minimum and starts to increase. This unfavorable pressure gradient decelerates the flow and even reverses it (the arrows with symbols in Fig. 6 show locations of corresponding vortex-breakdown bubbles and wavy regions in Figs. 2–4).

It follows that the circulatory zones observed in Figs. 2–4 are intimately related to the near-rod regions where the pressure gradient is unfavorable. The rod corotation completely suppresses vortex breakdown because it significantly reduces the unfavorable pressure gradients (e.g., see the $\mathrm{Re}_i=21$ curve in Fig. 6). A region of a small negative gradient of pressure retained at $\mathrm{Re}_i=21$ corresponds to a still wavy streamline but with no flow reversal region near point (i).

In contrast, the absolute values of negative pressure gradients become larger at $\mathrm{Re}_i=-12$ compared with those at $\mathrm{Re}_i=0$; these larger unfavorable pressure gradients enlarge the vortex-breakdown bubbles when the rod counter-rotates.

Our numerical results also agree with experimental observations [13] that the flow becomes time oscillating for $\mathrm{Re}_i<-14$. Figure 7 depicts oscillations of Γ_0, the value of circulation, $\Gamma=rv$, in the middle of the domain [at $r=(1-r_i)/2$ and $z=h/2$], at $\mathrm{Re}_i=-18$. The flow is clearly time periodic with small but saturated amplitude. To show that the most intense oscillations occur near the rod, we plot the in-

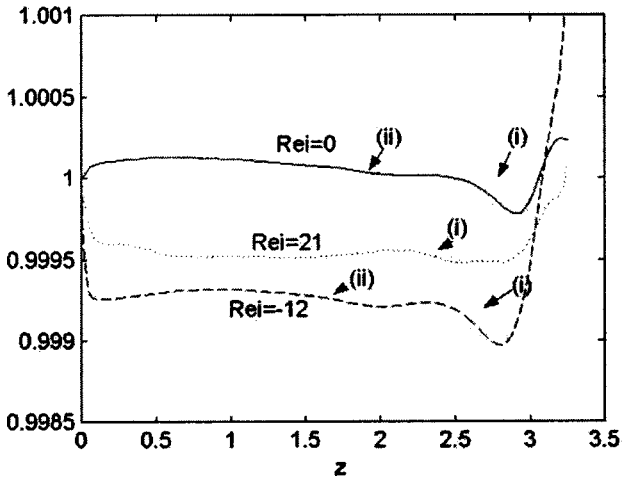

FIG. 6. Pressure along the rotating rod normalized by values at $z=0$ for three Re_i values shown near the curves. Symbols (i) and (ii) indicate locations of the VB bubbles or their remnants (in the $\mathrm{Re}_i=21$ case).

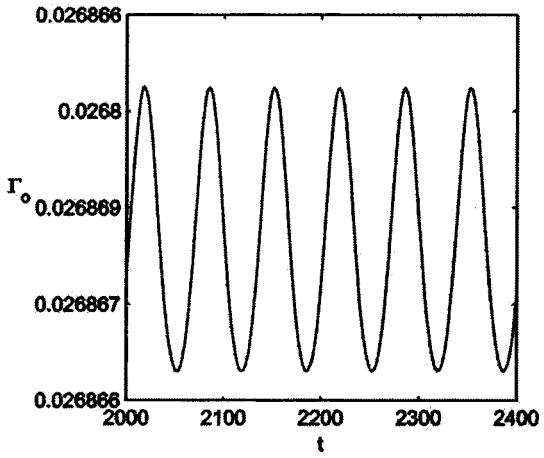

FIG. 7. Establishment of time-periodic oscillation in the flow with the counter-rotating rod at $\mathrm{Re}_i=-18$. Γ_0 is the circulation value at $r=(1-r_i)/2$ and $z=h/2$.

stantaneous streamline patterns at two different time values corresponding to the maximum [Fig. 8(a)] and minimum [Fig. 8(b)] of Γ_0 in Fig. 7. Figure 8 also indicates the periodic appearance and disappearance of the small near-rod circulatory region upstream of the larger one. For $\mathrm{Re}_i=-19$, the flow becomes weakly nonperiodic and for even smaller values of Re_i, the oscillations become strongly nonperiodic and intense.

Thus, our results agree with the experiment [13] that corotation (counter-rotation) being induced near the axis suppresses (enhances) VB. In addition, the numerical results clearly demonstrate (a) the role of unfavorable pressure gradients in the VB development, (b) the appearance of first periodic and then nonperiodic time oscillations as the counter-rotation intensifies, and (c) possible misidentification of bubbles by dye visualization.

This VB control can be significantly enforced by imposing a temperature gradient (ε). In the prior study [14], we

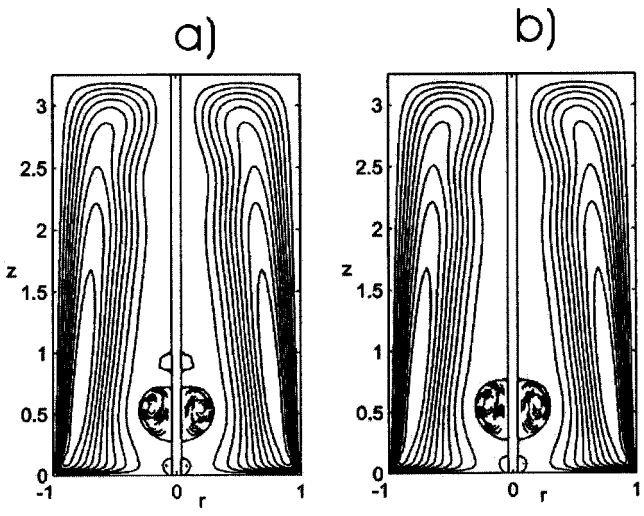

FIG. 8. Instantaneous streamline patterns at two different time values corresponding to the maximum (a) and minimum (b) of Γ_0 in Fig. 7. The top vortex ring near the rod appears and disappears periodically.

addressed the VB control by ε with no additional corotation or counter-rotation near the axis. Now we consider these two control means—the rod rotation and temperature gradient—acting together.

B. Addition of a temperature gradient

The underlying mechanism of the VB control by a temperature gradient is centrifugal and/or gravitational convection [14]. Here we focus on the centrifugal convection only motivated by the fact that centrifugal acceleration is significantly larger than gravity in practical flows.

An additional thermal-convection flow directed oppositely to the base flow suppresses VB while a coflow enhances the VB. In Sec. IV B we explore the effects of a temperature gradient for the counter-rotating central rod where the flow with no temperature gradient is still steady (at $\mathrm{Re}_i=-12$, Fig. 3).

1. Enhancing the VB and inducing oscillation by centrifugal convection

The axial gradient of temperature with $\varepsilon<0$ provides a control meridional flow of the same direction as that of the base flow. This coflowing intensifies the transport of angular momentum from the bottom disk toward the top lid and then toward the rod and thus strengthens concentration of the axial vorticity in the vortex core. This focusing results in two effects: (i) enlargement of VB bubbles and (ii) flow oscillation. Figure 9 shows the streamline patterns at $\mathrm{Re}_i=-12$ for a few values of ε: (a) $\varepsilon=0$ (steady flow, for comparison), (b) $\varepsilon=-0.3$ (still steady flow), and (c) $\varepsilon=-0.6$ (unsteady flow). We see that the size of the VB bubbles increases as ε decreases; this occurs even when the flow becomes unsteady. In addition, we plot Γ_0 as a function of time for $\varepsilon=0$, -0.4, and -0.45 in Fig. 10. This figure illustrates the development of time-periodic oscillation due to the control coflow intensifying the base meridional motion. Figure 10 also shows that the flow rotation around the axis (characterized by Γ_0) speeds up as well. For even smaller values of ε (<-0.45), the flow oscillation becomes nonperiodic.

Now we consider effects of the $\varepsilon>0$ temperature gradient.

2. Suppressing the VB by centrifugal convection

The direction of the $\varepsilon>0$ control flow is opposite that of the base flow outside the VB region. Such a control flow reduces the strength of the meridian motion and, therefore, the transport of the axial vorticity from the rotating bottom disk toward the upper lid. Another important feature of the control flow is its bulk convergence toward the axis [14] that reduces the spreading of streamlines away from the axis, typical of the base flow. Figure 11 shows the streamline patterns for (a) $\varepsilon=0.2$ and (b) $\varepsilon=0.7$. The upper bubble observed in Fig. 9(a) ($\varepsilon=0$) is completely suppressed even at $\varepsilon=0.2$ and the lower bubble shifts toward the bottom disk as ε increases. The meridian flows in Figs. 11(a) and 11(b) look similar, but they significantly differ in the strength of the meridian motion, which is reduced nearly by half when ε

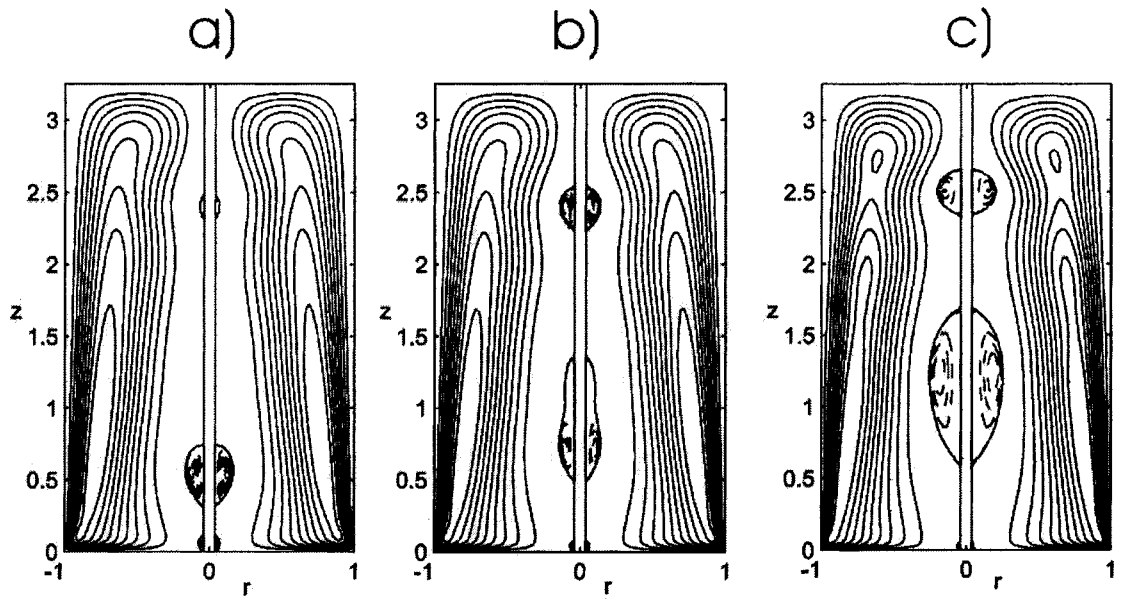

FIG. 9. Effect of the negative temperature gradient ($\varepsilon<0$) in addition to a counter-rotation ($\mathrm{Re}_i=-12$). The VB bubbles increase as ε decreases and the flow became unsteady: (a) $\varepsilon=0$ (steady flow), (b) $\varepsilon=-0.3$ (still steady flow), and (c) $\varepsilon=-0.6$ (unsteady flow).

increases from 0.2 to 0.7. This reduction and the corresponding decrease in the advection of the axial vorticity from the rotating disk have an important effect discussed below.

3. The development of centrifugal instability

The straightforward extrapolation of the flow trend as ε increases from 0 up to 0.7 [Figs. 9(a), 11(a), and 11(b)] might lead to a conjecture that the further increases in ε (beyond 0.7) should result in the total suppression of the VB bubble. However, our calculation at $\varepsilon=0.9$ has revealed the opposite effect: the flow becomes unsteady and several vortex rings appear near the rod [Fig. 11(c)].

We speculate that this flow development as ε increases from 0.7 to 0.9 occurs due to the centrifugal instability stimulated by the intense control counterflow. This scenario

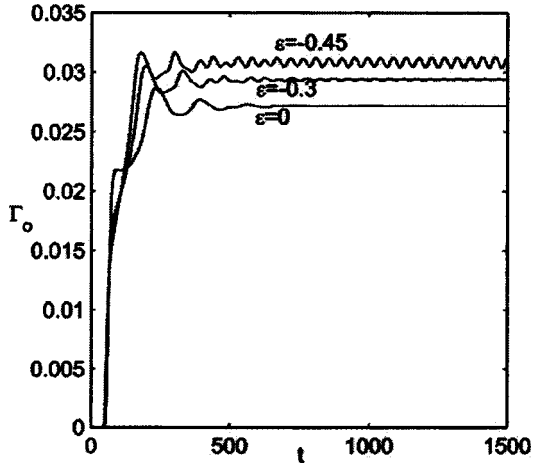

FIG. 10. Establishment of circulation (Γ_0) at $(1-r_i)/2$ and $z=h/2$ as time (t) increases for temperature gradient values (ε) shown near the curves and $\mathrm{Re}_i=-12$. When ε decreases below -0.4 the flow became unsteady.

is possible only due to combined effects of the $\varepsilon>0$ temperature gradient and the counter-rotating rod. Indeed, no instability and no vortex ring develop when ε increases without the rod counter-rotation [14]. Also, our calculations have revealed no instability and no vortex ring generation in the case of the corotating rod.

To verify the centrifugal mechanism of the instability observed, we explore the dependence of the Taylor number Ta on the temperature gradient, as ε increases. To this end, we define Ta in the following way. According to the Rayleigh criterion for the centrifugal instability [20], a flow can be unstable only if the squared circulation, $\Gamma=r^2v^2$, decreases as r increases. In the flow with the counter-rotating rod, Γ changes its sign at $r=\delta$, $r_i<\delta<1$, as r increases from r_i to 1. Accordingly, Γ^2 first decreases down to zero as r increases from r_i to δ, and then increases together with r in the interval, $\delta<r<1$.

The δ value depends on z in the way shown by curves $\Gamma=0$ in Fig. 12. This figure plot contours $\Gamma=\mathrm{const}$ for (a) $\varepsilon=0$ and (b) $\varepsilon=0.7$ at $\mathrm{Re}_i=-12$; the solid (dashed) lines are for $\Gamma>0$ ($\leqslant 0$). We see that the $\Gamma>0$ contours shrink while the $\Gamma<0$ region enlarges, especially near the bottom disk, as ε increases. We characterize the radial extent of the $\Gamma<0$ region by $\delta_{\max}$—the maximum value of δ as z varies—and introduce the Taylor number, $\mathrm{Ta}=|\Omega_i|R_iR_o(\delta_{\max}-r_i)/\nu$, where $R_o(\delta_{\max}-r_i)$ is a dimensional radial width of the $\Gamma<0$ flow region. As Ta exceeds some threshold value, the centrifugal instability should develop according to the Rayleigh condition (because $\partial\Gamma^2/\partial r<0$ in the $\Gamma<0$ region).

Figure 13 shows Ta as a function of ε at $\mathrm{Re}_i=-12$. The Taylor number nearly linearly increases with ε. Our numerical results show that multiple vortex rings appear near the rod and the flow becomes for $\mathrm{Ta}>75$ [Fig. 11(c)]. Compare this critical value of Ta with that known from the literature on the centrifugal instability. For the Taylor-Couette flow,

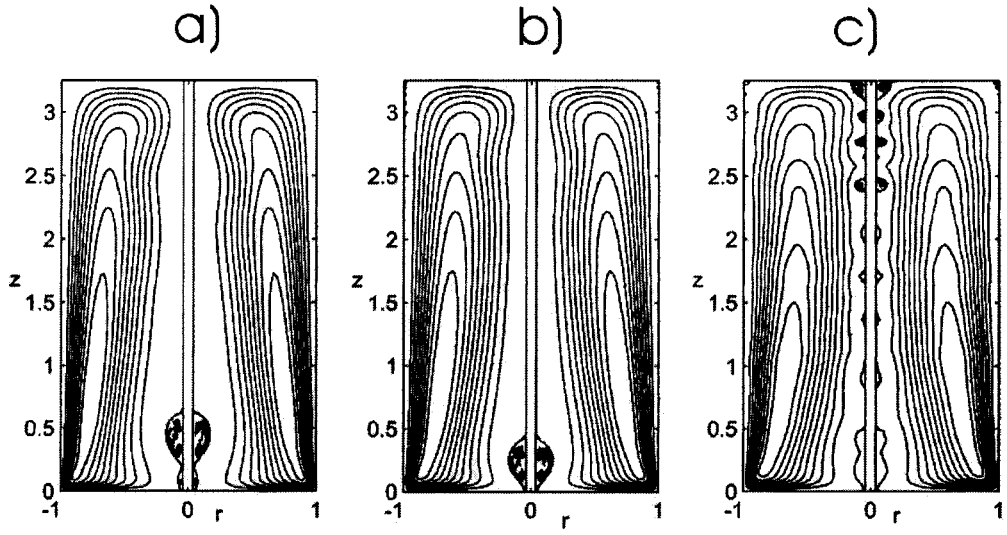

FIG. 11. Effect of the positive temperature gradient ($\varepsilon>0$) in addition to a counter-rotation ($\mathrm{Re}_i=-12$). As ε increases from (a) $\varepsilon=0.2$ to (b) $\varepsilon=0.7$, the vortex-breakdown bubbles decrease. As ε increases further, new vortex rings appear near the rod as shown in (c) $\varepsilon=0.9$, and the flow becomes unsteady.

where only the inner cylinder rotates and the outer/inner radius ratio is 0.5, the critical value of (64/9) $(\Omega_i R_i^2/\nu)^2$ is 3.31×10^4 according to both numerical [20] and experimental [21,22] results. This corresponds to Ta$=68$ which is close to the critical value of Ta ($=75$) in our flow. This agreement is surprisingly well though the flows are very different.

Let us discuss why the $\varepsilon>0$ temperature gradient causes the increases in Ta. At $\varepsilon=0$, the intense meridional motion transports the positive axial vorticity generated by the rotating disk toward the top lid, then toward the rod, and finally downward along the rod. This transport decreases the radial extent of the negative circulation due to annihilation of the positive and negative (generated by the rod counter-rotation) axial vorticities. Since the $\varepsilon>0$ temperature gradient weakens the meridional flow, the supply of the positive axial vorticity to the near-rod flow region decreases. Figure 12 clearly shows this effect: the $\Gamma>0$ contours shrink as the $\varepsilon>0$ temperature gradient increases, e.g., compare curves 1 in Fig. 12(a) and Fig. 12(b). The reduction of the positive axial vorticity naturally results in the increase of the radial extent of the negative circulation region, especially near the bottom where the supply of the positive axial vorticity by the meridional flow is minimal. Therefore, Ta grows and the centrifugal instability develops when Ta exceeds its critical value.

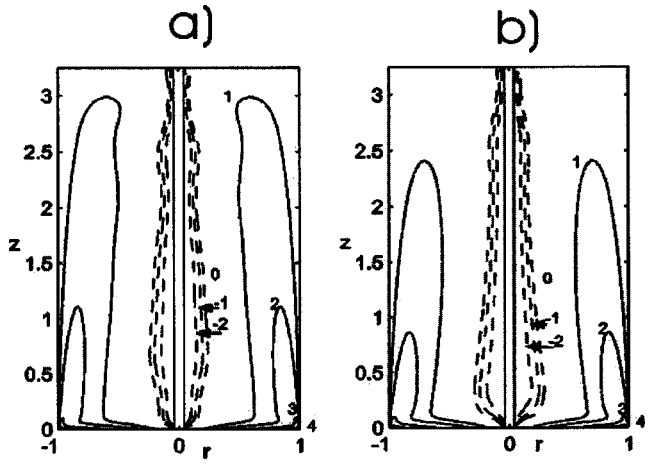

FIG. 12. Circulation contours at $\mathrm{Re}_i=-12$ and (a) $\varepsilon=0$ and (b) $\varepsilon=0.7$. Contours are solid (broken) for positive (zero and negative) circulation values: 1/30 (curve 1), 1/10 (curve 2), 1/3 (curve 3), 2/3 (curve 4) of $\Gamma_{\max}$, 0 (curve 0), 1/3 (curve -1), and 2/3 (curve -2) of $\Gamma_{\min}$.

V. CONCLUSIONS

Our investigation of the vortex breakdown (VB) control by adding near-axis rotation and temperature gradients can be summarized as follows.

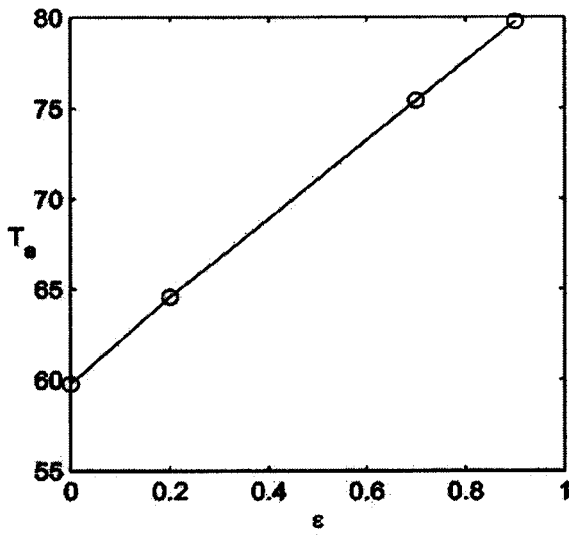

FIG. 13. The Taylor number (Ta) as a function of the temperature gradient (ε) at $\mathrm{Re}_i=-12$.

(1) The results for the flow with no temperature gradient ($\varepsilon=0$).

(i) Our simulations explain experimental observations [13] that near-axis corotation suppresses the VB, whereas the counter-rotation increases the size of the VB bubbles and makes the flow unsteady. Changes in the pressure distribution are crucial for the VB suppression and enhancement.

(ii) Corotation (counter-rotation) diminishes (enhances) the unfavorable pressure gradients—pressure increases downstream and thus suppresses (stimulates) the VB.

(iii) Our results show the possibility of bubble misidentification by dye visualization in the experiment.

(2) The addition of a negative temperature gradient ($\varepsilon<0$) induces a control meridional coflow, which enforces the counter-rotation effect, i.e., enhances the VB and makes the flow unsteady.

(3) A moderate positive temperature gradient ($0<\varepsilon<\varepsilon^*$) enforces the corotation effect, i.e., suppresses the VB, and diminishes the counter-rotation effect

(4) A strong positive temperature gradient ($\varepsilon>\varepsilon^*$) stimulates the development of centrifugal instability (the appearance of multiple vortex rings near the counter-rotating rod) and makes the flow unsteady. This occurs due to the reduction of positive axial vorticity transport from the rotating disk toward the axis. This leads to the radial enlargement of the counter-rotation region where the Rayleigh stability condition does not hold. In the corotation case, the centrifugal instability does not develop for any $\varepsilon>0$.

While these results explain the mechanism of VB control in the cylindrical-container flow, we expect that the conclusions listed above might be valid for a variety of natural and technological flows as well, because the effects of additional swirl and temperature gradients have generic physical mechanisms. It is clear that in practical systems, the rod rotation may not be feasible for control. In that case, an additional near-axis swirling (hot or cold) jet could help to achieve similar effects—the suppression or stimulation of the vortex breakdown and flow instability.

In practical flows, VB can be asymmetric (single or multiple helix) and unsteady. We expect that the effects of the additional swirl and temperature gradients in such flows should be similar to those revealed here. We plan to explore this issue using a three-dimensional code which is under development. On the other hand, a number practical and laboratory VB flows (e.g., [13]) are nearly axisymmetric and steady.

Based on the results reported above, we speculate that blowing of a corotating cold swirling jet should help to avoid a VB occurrence above a delta wing. Vice versa, a control counter-rotating hot jet could help to enhance mixing in vortex burners and thus to reduce harmful emissions.

ACKNOWLEDGMENT

This work has been partially supported by the Dirección General de Enseñanza Superior of Spain, Grant No. BMF2000-0528.

[1] M. V. Lowson, J. R. Aeronaut. Soc. **68**, 343 (1964).
[2] O. R. Burggraf and M. R. Foster, J. Fluid Mech. **80**, 685 (1977).
[3] A. K. Gupta, D. G. Lilley, and N. Syred, *Swirl Flows* (Abacus Press, Kent, England, 1984).
[4] M. P. Escudier, Prog. Aerosp. Sci. **25**, 189 (1988).
[5] R. P. Davies-Jones, in *Thunderstorms: A Social, Scientific and Technological Documentary*, edited by E. Kessler (University of Oklahoma Press, Norman, OK, 1983), Vol. 2, p. 297.
[6] V. Shtern and F. Hussain, Annu. Rev. Fluid Mech. **31**, 537 (1999).
[7] H. U. Vogel, Max-Planck-Institut für Strömungsforschung, Göttigen, Bericht., 1968, Vol. 6.
[8] M. Goldshtik, H. S. Husain, and F. Hussain, Phys. Rev. A **45**, 8611 (1992).
[9] F. Sotiropoulos, D. R. Webster, and T. C. Lackey, J. Fluid Mech. **466**, 215 (2002).
[10] F. Sotiropoulos, Y. Ventikos, and T. C. Lackey, J. Fluid Mech. **444**, 257 (2001).
[11] F. Sotiropoulos and Y. Ventikos, J. Fluid Mech. **426**, 155 (2001).
[12] E. Serre and P. Bontoux, J. Fluid Mech. **459**, 347 (2002).
[13] H. S. Husain, V. Shtern, and F. Hussain, Phys. Fluids **15**, 271 (2003).
[14] M. A. Herrada and V. Shtern, Phys. Fluids (to be published).
[15] M. A. Herrada, M. Pérez-Saborid, and A. Barrero, Phys. Fluids **15**, 2208 (2003).
[16] Z. Rusak and J. H. Lee, J. Fluid Mech. **461**, 301 (2002).
[17] C. Canuto, M. Y. Hussaini, A. Quarteroni, and T. A. Zang, *Spectral Methods in Fluid Dynamics* (Springer-Verlag, Berlin, 1988).
[18] S. K. Lele, Comput. Phys. **103**, 16 (1992).
[19] C. Hirsch, *Numerical Computation of Internal and External Flows*, 2nd ed. (Wiley, New York, 1997).
[20] S. Chandrasekhar, *Hydrodynamic and Hydromagnetix Stability* (Dover, New York, 1961).
[21] R. J. Donnelly, Proc. R. Soc. London, Ser. A **246**, 312 (1958).
[22] D. Fultz, Proc. R. Soc. London, Ser. A **258**, 101 (1960).